Robust Segmentation of the Luminal Border in Intravascular Ultrasound Using a Probabilistic Approach*

E.G. Mendizabal-Ruiz, M. Rivera[†], and I.A. Kakadiaris

Department of Computer Science
University of Houston
Houston, TX, 77204, USA
`http://www.cs.uh.edu`

Abstract

Intravascular ultrasound (IVUS) is a catheter-based medical imaging technique that produces cross-sectional images of blood vessels and is particularly useful for studying atherosclerosis. In this paper, we present a probabilistic approach for the identification of the luminal border in IVUS images. We tested our method on six 20 MHz and six 40 MHz IVUS pullback sequences, and we evaluated its performance by comparing the segmentation results of our method with manual segmentation by an expert observer and three other segmentation methods available in the literature. The performance of our method was quantified using Dice similarity, linear regression and Bland-Altman analysis. The results indicate the reliability and robustness of our method, and that the performance of our method is superior when compared with other existing methods. To the best of our knowledge, our method is the first to be robust with respect to different IVUS image appearance and changes on the visualization parameters within a sequence.

[†]Mariano Rivera is with Centro de Investigación en Matemáticas. Guanajuato, Gto. México.

Robust Segmentation of the Luminal Border in Intravascular Ultrasound Using a Probabilistic Approach*

E.G. Mendizabal-Ruiz, M. Rivera†, and I.A. Kakadiaris

Abstract

Intravascular ultrasound (IVUS) is a catheter-based medical imaging technique that produces cross-sectional images of blood vessels and is particularly useful for studying atherosclerosis. In this paper, we present a probabilistic approach for the identification of the luminal border in IVUS images. We tested our method on six 20 MHz and six 40 MHz IVUS pullback sequences, and we evaluated its performance by comparing the segmentation results of our method with manual segmentation by an expert observer and three other segmentation methods available in the literature. The performance of our method was quantified using Dice similarity, linear regression and Bland-Altman analysis. The results indicate the reliability and robustness of our method, and that the performance of our method is superior when compared with other existing methods. To the best of our knowledge, our method is the first to be robust with respect to different IVUS image appearance and changes on the visualization parameters within a sequence.

Index Terms

Probabilistic, Segmentation, IVUS, Optimization, Blood vessel.

I. INTRODUCTION

Complications attributed to cardiovascular disease (CVD) are currently the main cause of death worldwide [1]. It is known that the majority of adverse CVD-related events are due to coronary artery disease: a condition in which fatty lesions called plaques are formed on the walls of those vessels which nourish the heart with blood. Sudden rupture of a plaque may lead to a rapidly-progressing stenotic condition in which the blood supply is entirely cut off from a region of the heart. This may result in death.

Intravascular ultrasound (IVUS) is a catheter-based medical imaging technique capable of providing high-resolution, cross-sectional images of the interior of blood vessels in real time; it allows the collection of morphological information about the vessel and any plaque.

The IVUS catheter consists of either a solid-state or a mechanically-rotated transducer which transmits ultrasound pulses and receives a reflected signal (i.e., A-line) over each radial scan (Fig. 1(a)) at a discrete set of angles. Commonly, 240 to 360 A-line signals are obtained per rotation. Then, the envelopes of these signals are computed, compressed, stacked along the angular direction, and mapped into 8-bit gray scale to form an image known as a polar B-mode image (Fig. 1(b)). Finally, the polar B-mode image is geometrically transformed to obtain the familiar disc-shaped image known as a Cartesian B-mode image (Fig. 1(c)).

Segmentation of IVUS images refers to the delineation of the lumen/intima and media/adventita borders (Fig. 2). This process is necessary for assessing the vessel and plaque characteristics. This information is very important for making decisions such as whether a stent is needed to restore blood flow in an artery and the required characteristics of this stent.

Given that IVUS sequences may be hundreds to thousands of frames long, the manual segmentation of a complete sequence is prohibitively time-consuming. Moreover, manual segmentation may suffer from inter- and intra-observer variability due to its high level of subjectivity. Studies show that large differences (up to 20%) in the cross-sectional area of luminal segmentations provided by the same observer may be possible [2]. Thus, a robust automatic segmentation method for IVUS images is needed to overcome these limitations. However, automatic segmentation of IVUS images remains an open problem because of (i) the different artifacts that can appear in the IVUS images

---

†Mariano Rivera is with Centro de Investigación en Matemáticas. Guanajuato, Gto. México.
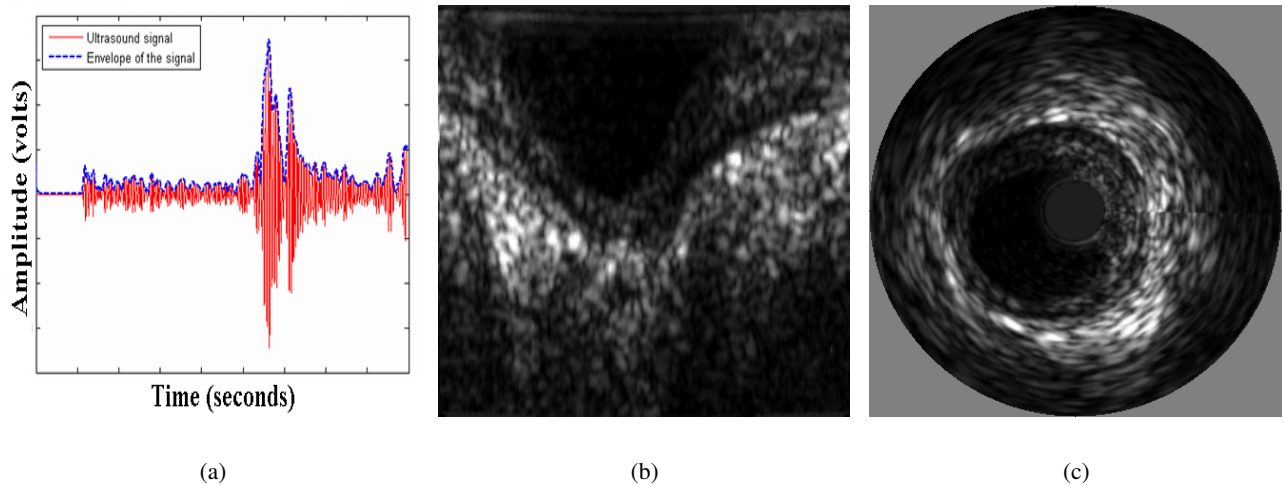
Fig. 1. Depiction of (a) an A-line signal and its envelope, (b) a B-mode polar IVUS image, and (c) a B-mode Cartesian IVUS image.
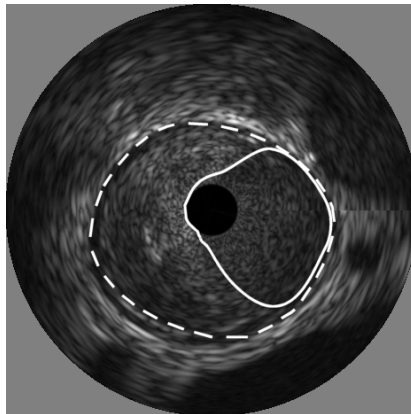

Fig. 2. Depiction of lumen/intima and media/adventitia borders (straight and dotted line, respectively) on a sample IVUS image

(e.g., catheter rotation, shadows, speckle noise, and guidewire artifacts), and (ii) the variability on the appearance of the IVUS images which depends on the settings of the IVUS system (i.e., frequency of the transducer), and the image-generation parameters (i.e., time-gain compensation (TGC), compression, brightness, and contrast) that are subjectively adjusted by the interventionist.

In this paper, we present a robust probabilistic approach for the segmentation of the luminal border on IVUS images. In our proposed method, *a priori* information is incorporated by using the prediction of a Support Vector Machine (SVM) classifier model that is trained using a small number of samples from lumen and non-lumen regions provided by the user on the first frame of the sequence to be segmented. This step allows our method to autocalibrate making it capable of working with IVUS images from different frequencies (i.e., 20 and 40 MHz) without the need of adjusting any parameter, and it makes the method robust to the problem of variability of IVUS image appearance. Additionally, our method includes a step in which changes in appearance within the sequence are automatically detected and the SVM model is adjusted. Moreover, the probabilistic formulation of our method overcomes the limitations related to catheter rotation, speckle noise, shadows, and guidewire artifacts.

Specifically our contributions are: (i) a segmentation method that is robust with respect to the variability of IVUS images and its possible in-sequence variability, and (ii) a novel optimization strategy that linearly combines the direction of two optimization methods to stabilize the convergence.

The rest of the paper is organized as follows: Section 2 presents previous work in IVUS segmentation, while Section 3 presents the steps of our segmentation method. Section 4 presents the results obtained with our method,

A preliminary version of this method has been previously presented in [3]

and Sections 5 and 6 present our discussion and conclusions, respectively.

II. PREVIOUS WORK

Automated segmentation of IVUS sequences has been a topic of interest since at least the early 1990. Many of the first approaches were based on the use of local properties of the image such as pixel intensity and gradient information (edges) combined with computational methods including graph search [4], [5], [6], active surfaces [7], active contours [8], and neural networks [9]. In later approaches, segmentation was accomplished by the use of region and global information including texture [10], gray level variances [11], [12], contrast of regions [13], statistical properties of the image [14], temporal information (3D segmentation) [15], and discrete wavelet decomposition [16].

Most recently, a shape-driven method for lumen and media-adventitia segmentation was introduced by Unal *et al.* [17]. In this work, the lumen and media-adventitia contours were constrained to a smooth, closed geometry. Then, a shape space was built using training data and principal component analysis. Finally, segmentation was performed on this shape space by the minimization of an energy function using nonparametric probability densities with global measurements. Taki *et al.* [18] proposed a method for the identification of the vessel borders. This method consisted of first preprocessing the IVUS images, and then geometric and parametric models were deformed using edge information. Downe *et al.* [19] introduced a method where principal component analysis was used for pre-processing, while active contour models were used to provide an initial segmentation for a 3D graph search method. Multilevel discrete wavelet frames decomposition was used by Papadogiorgaki *et al.* [20] to generate texture information that was used along with the intensity information for contour initialization. Similarly, Katouzian *et al.* [21] presented a method where texture information was extracted using a discrete wavelet packet transform. Then, pixels were classified as lumen or non-lumen using k-means clustering. Finally, the contour was parameterized using a spline curve. Ciompi *et al.* [22] presented a method in which segmentation was tackled as a classification problem and solved using an error correcting output code technique. In that work, contextual information was exploited by means of conditional random fields computed from training data. Wennogle *et. al* [23] proposed improvements over an existing method presented in [15] consisting of a preprocessing step to remove motion artifacts, a new directional gradient velocity term, and a post-processing level-set method. Cardinal *et al.* [24] presented a multiple interface 3D fast-marching method that is based on a combination of gray level probability density functions and the intensity gradient. The segmentation method included an interactive initialization procedure of the external vessel wall border.

In particular, most of the method that employ edge information are designed to work with IVUS sequences acquired with low frequencies (i.e., 10 to 20 MHz) and may not work with higher frequency images (i.e., 30 to 40 MHz) since these methods rely in the fact that at low frequencies the blood presents low acoustic impedance and therefore there is a large contrast between lumen and wall tissues. Moreover, the major limitation of these methods is that artifacts or excessive speckle noise in the images can be interpreted as an arising from the change of interface resulting in an incorrect segmentation. The main disadvantage of 3D-based methods is the requirement of an accurate alignment of the images to compensate the motion artifacts produced by the movement of the heart. Since registration of IVUS images remains an open problem, current methods attempt to alleviate these motion artifacts by using electrocardiogram-based or image-based gating. However, this results in a loss of information since many frames have to be ignored. In general, the major limitation for all IVUS segmentation methods is that apart from the frequency of operation, the settings of the IVUS systems such as TGC, compression, brightness, and contrast, have a strong influence on the appearance of the B-mode images [25] (Fig. 3). These settings are subjectively selected by the interventionist, and may change several times during the acquisition [26]. Since most of the current IVUS segmentation methods rely in the similar appearance of all the frames within the sequence to be segmented (especially for 3D-based methods), these are designed and tested employing sequences generated with specific system settings. Therefore, these methods may not work appropriately on sequences generated with different settings or a different IVUS system, and they are very likely to fail on the cases where the interventionist perform changes on the visualization parameters during the acquisition of the sequence.

III. METHODS

Similarly to previous approaches, we employ the B-mode polar IVUS image representation. This choice makes the problem friendlier due to the 1D appearance of the lumen contour (Fig. 4). In this representation, the horizontal
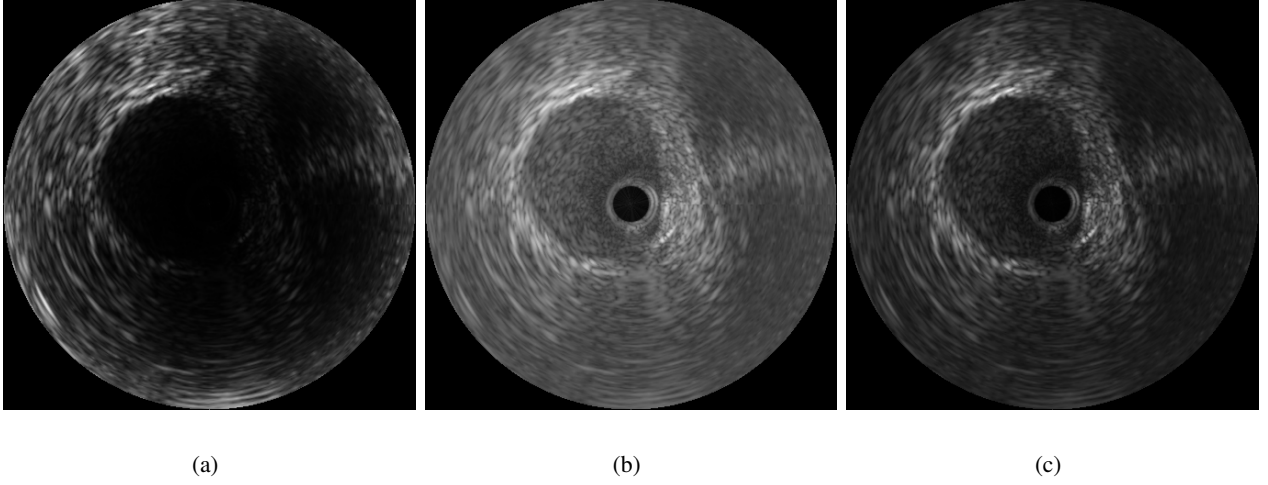
(a) (b) (c)

Fig. 3.   Examples of the same IVUS image obtained with different B-mode transformation parameters.

axis corresponds to the angular position of the transducer, while the vertical axis corresponds to radial penetration by the ultrasound beam. Therefore, the intensity value of a pixel can be defined as $I(r, \theta)$ where r and θ corresponds to the radius and angle, respectively (Fig. 5). We define $S(\theta, \vec{C})$ to be the curve that represents the change of interface between lumen and vessel wall. This function is parameterized by a function that depends on θ and the parameters $\vec{C}$.
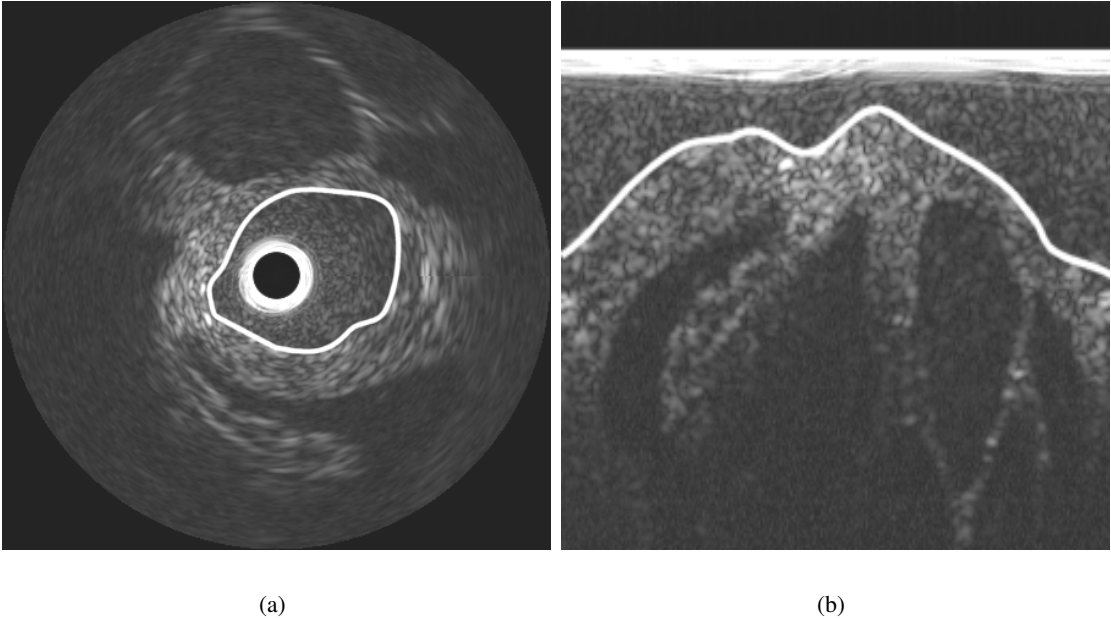

(a) (b)

Fig. 4.   Depiction of lumen contour in (a) Cartesian and (b) polar B-mode representations.

A. Contour parameterization

In the majority of cases the shape of the vessel's wall is smooth. Therefore, we require the contour described by $S(\theta, \vec{C})$ to be smooth as well. Moreover, we know that a polar B-mode IVUS image is periodic with respect to the horizontal axis. Therefore, the periodicity of the contour is also a requirement. In this work, we have chosen to parameterize the function that represents the lumen contour using Fourier series since it provides a periodic curve
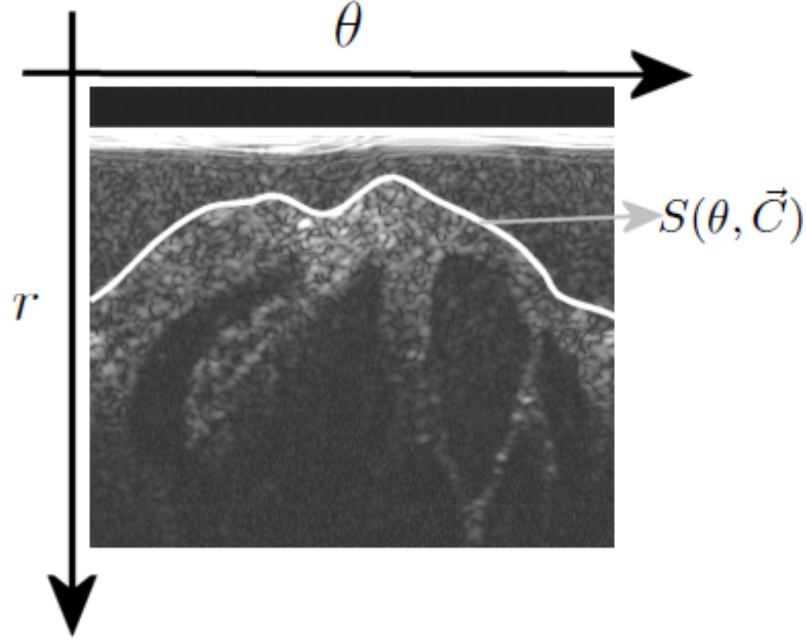
Fig. 5.   Depiction of contour parametrization on the B-mode polar image.

in which smoothness can be controlled by the number of coefficients N_k. The lumen contour is given by:

$$S(\theta, \vec{C}) = \frac{a_0}{2} + \sum_{k=1}^{N_k} \left[a_k \cos\left(\frac{k 2\pi\theta}{N}\right) + b_k \sin\left(\frac{k 2\pi\theta}{N}\right) \right] .$$ (1)

Here, N corresponds to the number of angles (i.e., width of the image), and

$$\vec{C} = [a_0, a_1, ..., a_{N_k-1}, b_1, ..., b_{N_k-1}]^T.$$

are the Fourier coefficients that control the shape of the curve.

B. Cost function

In our method, the lumen segmentation problem consists of finding the optimum parameters $\vec{C}^*$ such that the curve $S(\theta, \vec{C}^*)$ corresponds to the interface between lumen and vessel wall. The formulation we introduce to solve this problem was inspired by the probabilistic segmentation method proposed by Rivera *et al.* [27]. In their paper, the authors posed the image segmentation problem as the optimization of a cost function formulated using Markov random fields with a Bayesian approach. Intuitively, this method tries to find the best balance between the costs of assigning a certain probability to each pixel x to belong to each of the M classes, based on some prior knowledge $v_k(x)$ (i.e., likelihood for each class). The cost function is given by:

$$U(b) = \sum_x \sum_{k=1}^{M} b_k(x)^2 (-log(v_k(x)) - \mu) + \gamma \sum_{<x,y>} ||b(x) - b(y)||^2 ,$$ (2)

where $b_k(x)$ corresponds to the probability of the membership of the pixel x to the class k, and μ and γ are parameters that control the entropy and granularity of the segmentation result, respectively. Then, the task is to compute the vector field $b = \{b_1, b_2, ..., b_M\}$, such that $b_k(x) \geq 0$ and $\sum_{k=0}^{M} b_k(x) = 1 \forall x$.

For our segmentation problem, we can assume that all the pixels inside (i.e., above) the lumen contour correspond to lumen, while those pixels outside (i.e., below) this contour correspond to non-lumen. Then, the class for each pixel can be found by the sign of the distance $d(r, \theta)$ between the pixel (r, θ) and the curve $S(\theta, \vec{C})$:

$$d(r, \theta, \vec{C}) = f(\theta, \vec{C}) - r .$$ (3)

h

Name	Kernel				
Levels (L5)	[1	4	6	4	1]
Edges (E5)	[-1	-2	0	2	1]
Spots (S5)	[-1	0	2	0	-1]
Waves (W5)	[-1	2	0	-2	1]
Ripples (R5)	[1	-4	6	-4	1]

If the value of $d(r, \theta)$ is positive, then the pixel belongs to lumen, otherwise it belongs to non-lumen. We propose to use a sigmoid function to define the probability of each pixel in the image to belong to lumen $P_l(r, \theta)$ depending on its distance to the curve:

$$P_l(r, \theta, \vec{C}) = \frac{1}{1 + e^{-\lambda d(r, \theta, \vec{C})}} \ . \tag{4}$$

Using this formulation, pixels far above the contour will have a higher probability of belonging to lumen, while the pixels far below the contour will have probability close to zero. For the pixels near the contour, depending on the value of λ, the probability of belonging to lumen will be close to 0.5. Since we only have two classes, the probability of a pixel to belong to non-lumen is given by: $P_w = (1 - P_l(x))$.

In our problem, the entropy is related to the sharpness of the transition between classes (from $P \approx 1$ to $P \approx 0$) and is controlled by the parameter λ. In addition, the granularity does not pose a problem since the contour f defines just two regions. Therefore, we can set the values of μ and γ to zero. Moreover, since the square of a sigmoid function can be emulated with the same sigmoid function using different values of λ, we can rewrite Eq. (2) as:

$$U(\vec{C}) = \sum_r \sum_\theta [P_l(r, \theta, \vec{C})][-log(v_l(r, \theta))] + [1 - P_l(r, \theta, \vec{C})][-log(v_n(r, \theta))] \ , \tag{5}$$

where $v_l(r, \theta)$ and $v_n(r, \theta)$ represent the *a priori* information (i.e., likelihood of the pixel to belong to the lumen and non-lumen, respectively).

C. Likelihood estimation

To estimate the likelihood of each pixel to belong to lumen or non-lumen, it would be necessary to have a model that describes how the intensity values of each pixel are generated depending on its class. Since we do not have these models, it is necessary to approximate them. While in 20 MHz IVUS data the lumen tends to appear darker as compared to the wall, in 40 MHz data the lumen region presents some texture patterns because of the large intensity variation in the lumen mostly due to speckle noise. Therefore, it is necessary to add texture information in the *a priori* term. In our work, the likelihoods for lumen and non-lumen for each pixel are approximated using the class and probability estimates given by an SVM classifier using texture features.

1) Texture features: Laws' texture measures are a well known, widely used class of textural image descriptors [28] and enjoy continued use today in spite that it has been almost three decades since their development. Reasons for their longevity may include their relatively simple implementation, the fact that they mimic the behavior more advanced methods, and their success with so-called microtextures (i.e., fine-grained, high-frequency textures whose salient components are near to image resolution). Laws' texture features are generated from an image by first convolving the image with a number of specialized kernels. These kernels are in the majority of cases 5×5 (level 5), though others were proposed which do not currently find widespread use. The level 5 kernels are produced by taking the outer product of all the combinations of the basis one-dimensional level-5 convolution kernels (Table I). The 2D kernels are assigned a string mnemonic $k_L k_E^T$ (e.g., Kernel L5E5 is generated by convolving vertical kernel L5 by horizontal kernel E5). A total of 25 images are formed by convolving the original 2D images with the convolution kernels.

After convolving an image with these kernels, it is necessary to convert each of the resulting 25 images L_l into a measure of texture energy E_l. This is accomplished by a windowing operation in which the value of every pixel

x is replaced by the absolute value of the sum of the pixel values in a 5×5 window W_x centered in the pixel x. This is:

$$E_l(x) = \sum_{y \in W_x} |L_l(y)|,$$

These texture energies are used to form a 25-dimensional feature vector that will characterize the class of each pixel.

2) Support vector machines classifier: SVM is a class of binary supervised learning methods that are commonly used for classification and regression. SVMs process the data by mapping all samples features into a high dimensional space defined by a kernel. In this high dimensional space, the data may be linearly separated by a single boundary defined by a hyperplane where support is given by selected samples in the data (support vectors). To increase the probability of correct classification it is desirable to have the decision boundary at a maximum possible distance from the samples. The distance between the support vectors and the decision boundary is called the margin. The goal of SVM, is to find a separating hyperplane that would result in the largest margin. Once the optimal hyperplane function is computed, any new sample can be classified by mapping its features into the same space defined by the kernel and then evaluating in the discriminant function. In addition to the class of a given sample, it is possible to compute the posterior probability from the SVM output [31]. In this work, we use the SVM implementation provided in the libSVM library [32].

3) Likelihood approximation: We construct on the assumption that the texture of the regions of interest are similar among the IVUS sequences. Then, the likelihood estimation process can be divided into two steps: training and deployment.

Training: In the training step we require the user to select samples of lumen and non-lumen regions from the first frame of the sequence to be segmented (Fig. 7). We compute the texture energies of the frame using the Law's filters as described previously and a feature vector $\vec{S} \in R^{25}$ is formed for each pixel on the frame. We associate all the samples with a corresponding class according to the annotation by the user. From all the collected lumen and non-lumen samples, only ξ_1 are randomly selected to form a training set. The optimal SVM parameters c and γ are found using a grid search with 5-fold cross-validation. Next, a predicting model is obtained by training the SVM using the training set and the computed optimal parameters. It is important to note that the catheter and ringdown artifact (i.e., the bright halo around the catheter) may cause misclassifications of the regions of interest (Fig. 6). Fortunately, the locations of the catheter and the ringdown artifact remains constant among the sequence. Thus, we require the user to also provide the position of the outer-most visible ringdown artifact and the likelihood of this region to belong to blood is set to one since we know that this region corresponds to blood in reality.

Deployment: For each of the frames to be segmented, texture energies are computed to form a feature vector for each of the pixels in the image. Then, the classification of each pixel using the predicting SVM model is performed resulting on a class and a probability for this class for each pixel. Finally, this information is used as the likelihoods for blood and non-blood, $v_l(r, \theta)$ and $v_n(r, \theta)$, respectively (Fig. 8).

D. Optimization

To deform the lumen contour until it reaches the best segmentation, it is necessary to find the values of $\vec{C}^*$ that minimize the cost function of Eq. (5). In this work, we propose to employ a line search method for this minimization. In a line search method, the optimal value $\vec{x}^*$ for a function $f(\vec{x})$ is computed iteratively. At every iteration k, the new value for $\vec{x}_{k+1}$ is computed by

$$\vec{x}_{k+1} = \vec{x}_k + \alpha_k \vec{p}_k , \tag{6}$$

where $\vec{p}_k$ is a descent or search direction and α_k is the step size at the iteration k. The value of α_k can be computed in a variety of ways. A popular inexact line search condition stipulates that α_k should give *sufficient decrease* on the objective function, as measured by the following inequality:

$$f(\vec{x}_k + \alpha_k \vec{p}_k) \leq f(\vec{x}_k) + u_1 \alpha_k \nabla f(\vec{x}_k)^T \vec{p}_k , \tag{7}$$

for some constant $u_1 \in (0, 1)$.

For more information regarding the theory of SVM we encourage the reader to consult [30]
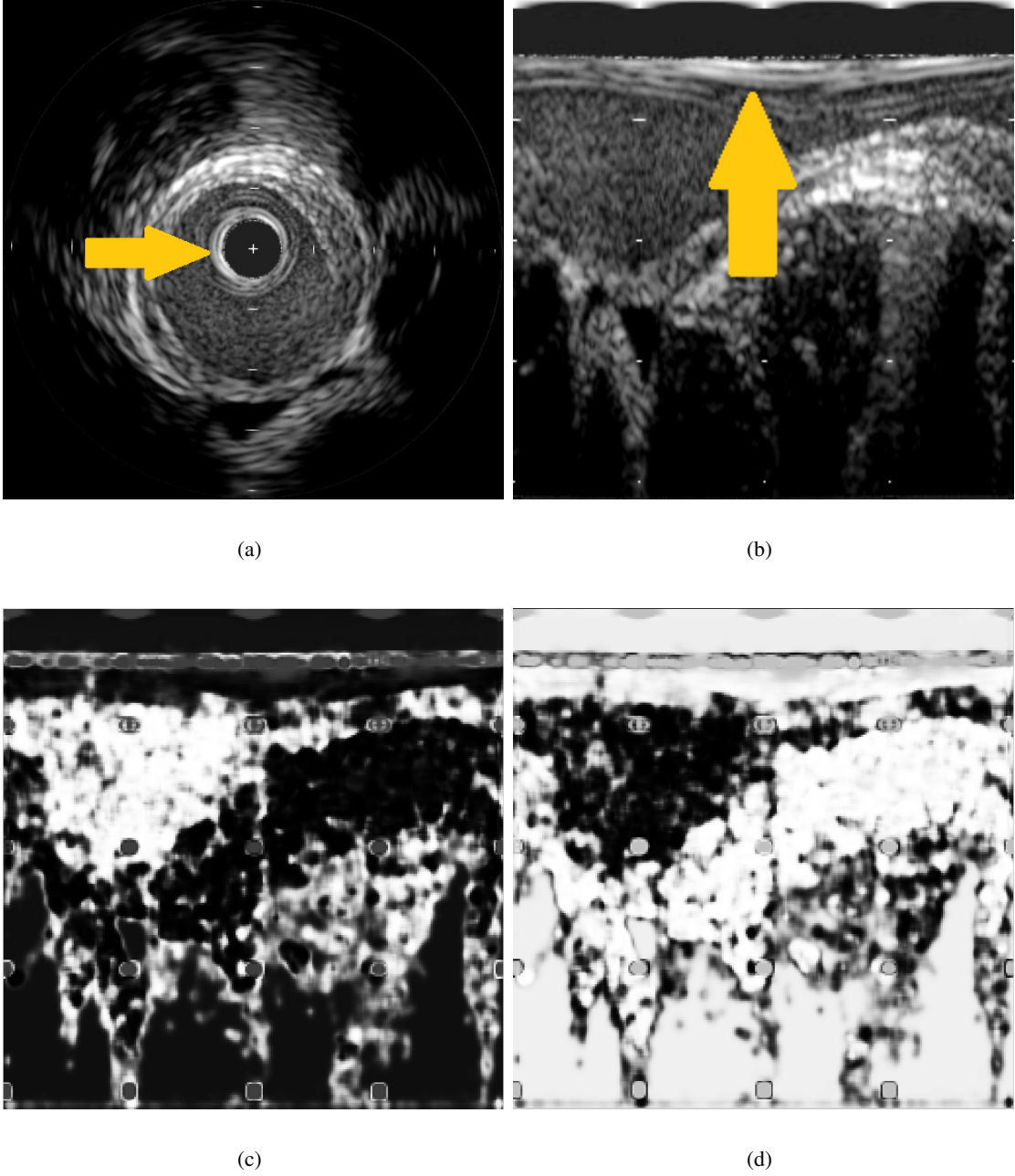
Fig. 6. Examples of (a) the first frame of a sequence, (b) its corresponding annotations of blood and non-blood regions by the user, and depictions of the likelihoods for (c) blood and (d) non-blood as computed using the SVM classifier.

Since this condition may be satisfied for some small values of α_k, it is necessary to introduce a second condition to ensure that the algorithm makes reasonable progress. This second condition requires α_k to satisfy:

$$\nabla f(\vec{x}_k + \alpha_k \vec{p}_k)^T \vec{p}_k \geq u_2 \nabla f(\vec{x}_k)^T \vec{p}_k \ , \tag{8}$$

for some constant $u_2 \in (u_1, 1)$. Both equations (7) and (8) are known collectively as the **Wolfe Conditions** [33].

For selecting the descent direction $\vec{p}$ at each iteration we have several options. We will discuss two such options below.

The steepest descent method; One of the simplest ways to solve this problem is by using the steepest descent method [33]. The steepest descent method is a line search method that iteratively moves along a search direction given by $\vec{p}_k^G = -\nabla f(\vec{x}_k)$ for an objective function $f(\vec{x})$. Although this method is robust and guarantees convergence
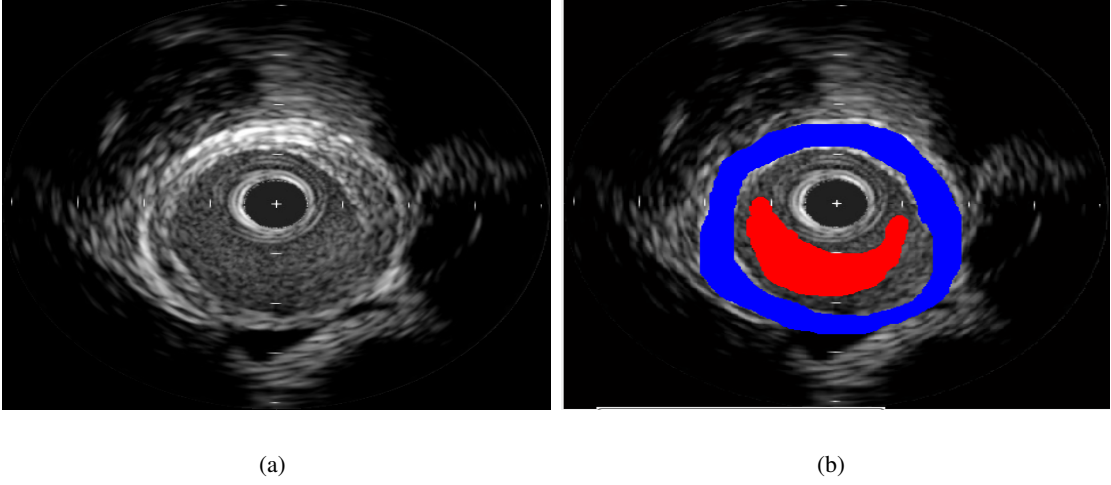
Fig. 7. Examples of (a) the first frame of a sequence, and (b) its corresponding user annotation for blood and non-blood (red and blue, respectively).
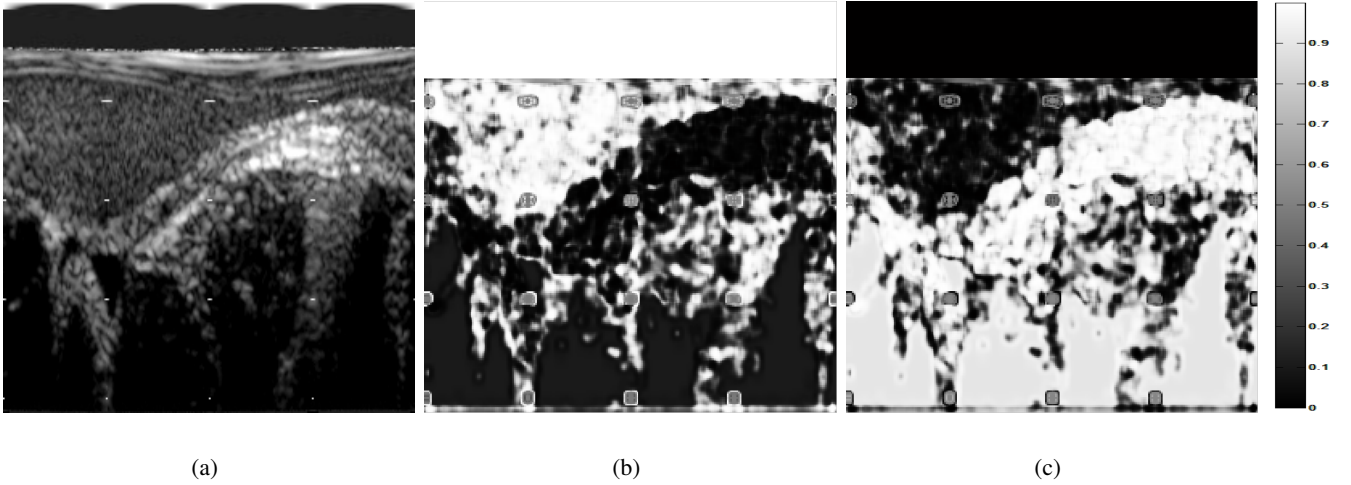

Fig. 8. Examples of (a) a polar IVUS frame, and its likelihood for (b) blood and (c) non-blood as computed by the SVM classifier.

to a local minimal, the main disadvantage is that this method may take a large number of iterations (i.e., time) to converge to the solution.

Broyden-Fletcher-Goldfarb-Shanno method: The **BFGS** method [33] converges to a solution faster when compared to steepest descent since it incorporates second order information. This method is used to solve unconstrained nonlinear optimization problems by using first and second order derivatives to find the point at which the gradient of the function is equal to zero. In this method, the search direction $\vec{p}_k$ at each iteration k is given by the solution of the equation:

$$B_k \vec{p}_k = -\nabla f(\vec{x}_k) \; , \tag{9}$$

where the matrix B_k is a positive definite approximation to the Hessian for each iteration.

The BFGS algorithm is efficient since, instead of computing B_k from scratch at every iteration, it is updated in a simple manner by taking into account the curvature measured in the most recent step. Let's assume that we have generated $\vec{x}_{k+1}$ and we wish to construct a quadratic model $m_{k+1}(\vec{p})$ using Taylor expansion:

$$m_{k+1}(\vec{p}) = f(\vec{x}_{k+1}) + \nabla f(\vec{x}_{k+1})^T \vec{p} + \frac{1}{2} \vec{p}^T B_{k+1} \vec{p} \; .$$

One reasonable requirement for B_{k+1}, based on the knowledge gained during the latest step, is that the gradient of m_{k+1} should match the gradient of the objective function $f(\vec{x}_k)$ at the last two iterations k and $k+1$. Since

$\nabla m_{k+1}(0)$ is precisely $\nabla f(\vec{X}_{k+1})$, the second of these conditions is satisfied by construction. The first condition can be written as

$$\nabla m_{k+1}(-\alpha_k \vec{p}) = \nabla f(\vec{x}_{k+1})^T - \alpha_k B_{k+1}\vec{p} = \nabla f(\vec{x}_k) .$$

By rearranging, we obtain:

$$B_{k+1}\alpha_k \vec{p} = \nabla f(\vec{x}_{k+1}) - \nabla f(\vec{x}_k) . \tag{10}$$

To simplify the notation, it is useful to define the vectors:

$$\vec{s}_k = \vec{x}_{k+1} - \vec{x}_k, \quad \vec{y}_k = \nabla f(\vec{x}_{k+1}) - \nabla f(\vec{x}_k) , \tag{11}$$

so that (10) becomes:

$$B_{k+1}\vec{s}_k = \vec{y}_k . \tag{12}$$

We refer to this formula as the *secant equation* [33]. Given the displacement $\vec{s}_k$ and the change of gradients $\vec{y}_k$, the secant equation requires that the symmetric positive definite matrix B_{k+1} maps $\vec{s}_k$ into $\vec{y}_k$. This will be possible only if $\vec{s}_k$ and $\vec{y}_k$ satisfy the *curvature condition*

$$\vec{s}_k^T \vec{y}_k > 0 , \tag{13}$$

as is easily observed by multiplying equation (12) by S_k^T. When $f(\vec{x}_k)$ is strongly convex, the inequality (13) will be satisfied for any two points ($\vec{x}_k$ and $\vec{x}_{k+1}$). However, this condition will not always hold for non-convex functions. In this case, we need to enforce (12) explicitly by imposing restrictions on the line search procedure that chooses α. The condition (12) is, in fact, guaranteed to hold if one impose the Wolfe Conditions on the line search.

To determine B_{k+1}, we must solve the problem

$$\min_B \|B - B_k\| \tag{14a}$$

$$\text{subject to} \quad B = B^T, \ B\vec{s}_k = \vec{y}_k , \tag{14b}$$

where $\vec{s}_k$ and $\vec{y}_k$ satisfy (13) and B_k is symmetric and positive definite. Using the weighted Frobenius norm, the unique solution of (14) is given by (see [33] for more details):

$$B_{k+1} = (I - \gamma_k \vec{y}_k \vec{s}_k^T)B_k(I - \gamma_k \vec{s}_k \vec{y}_k^T) + \gamma_k \vec{y}_k \vec{y}_k^T , \tag{15}$$

with

$$\gamma_k = \frac{1}{\vec{y}_k^T \vec{s}_k} . \tag{16}$$

Now we must solve the system in (9). The computation of B_k^{-1} can be made by regular methods. However, it is also possible to directly compute the inverse of the Hessian approximation B_k^{-1} by the Sherman-Morrison-Woodbury formula. Hence:

$$H_{k+1} = (I - \rho_k \vec{s}_k \vec{y}_k^T)H_k(I - \rho_k \vec{y}_k \vec{s}_k^T) + \rho_k \vec{s}_k \vec{s}_k^T , \tag{17}$$

where

$$\rho_k = \frac{1}{\vec{y}_k^T \vec{s}_k} . \tag{18}$$

Now the descent direction can be directly computed with

$$\vec{p}_k^B = -H_k \nabla f(\vec{x}_k) . \tag{19}$$

Unfortunately, since in our problem the cost function may have many local minima (mostly due to the similarity between the gray level of lumen and some parts of the wall), solving a problem with this method could leads us to an incorrect segmentation if the updating step is too large (in an extreme case, a too large step may locate the class border out of the IVUS image). In other words, the steepest descent method is robust but slow, while BFGS is fast but may over-segment. Therefore, we propose an optimization method that linearly combines the descent directions from steepest descent ($\vec{p}^G$) and BFGS ($\vec{p}^B$) methods. We will refer to this method as **GB optimization**.

1) GB optimization: One can note that the direct computation of the inverse of the Quasi-Hessian, H, is an advantage of the BFGS algorithm over other Newton algorithms such as Levenberg-Marquart (LM), but the main reason why we have chosen BFGS over LM is the information obtained from the product $\vec{s}_k^T \vec{y}_k$. On the curvature condition (Eq. (13)), when $\vec{s}_k^T \vec{y}_k$ is greater than zero, the curvature of the function becomes more positive as the descent approaches to a minimum. However, if $\vec{s}_k^t \vec{y}_k < 0$, the curvature condition is not satisfied and a better descent direction is the negative gradient (i.e., steepest descent direction). Additionally, we note that for small values of the product $\vec{s}_k^t \vec{y}_k$, the computation of the update formula for the Hessian, or its inverse, is non-defined (the function is not locally convex). Then, by design there is more confidence in the BFGS descent direction if the ρ value is large and positive. On the other hand, for $\rho \approx 0$, the confidence in $\vec{p}_k^B$ is smaller and we prefer the steepest descent direction $\vec{p}_k^G$. Based on this analysis, we propose to compute the descent direction as a convex linear combination of both descent directions:

$$
\begin{aligned}
\vec{p}_{k+1}^{GB} &= -[\psi(\rho_k)\vec{p}_k^B + (1 - \psi(\rho_k))\vec{p}_k^G] \\
&= -[(\psi(\rho_k)H_k \nabla f(\vec{x}_k)) + ((1 - \psi(\rho_k))\nabla f(\vec{x}_k))].
\end{aligned}
\tag{20}
$$

Then,

$$
\vec{p}_{k+1}^{GB} = -(\psi(\rho_k)H_k + (1 - \psi(\rho_k))I)\nabla f(\vec{x}_k),
\tag{21}
$$

where the function that controls the contribution of each descent direction $\psi(\rho)$ is defined as:

$$
\psi(\rho) = \begin{cases} 0 & \text{if } \rho < 0 \\ \frac{\rho^2}{K + \rho^2} & \text{otherwise .} \end{cases}
\tag{22}
$$

Note that in Eq. (21) the first is the Hessian inverse and the second is an adaptive diagonal term that enforces an energy descendent direction. Differently from the LM algorithm, our diagonal term is automatically adapted and the Hessian inverse in more efficiently computed.

Then, the search direction is given by:

$$
\hat{\vec{p}}_k^{GB} = \frac{\vec{p}_k^{GB}}{\|\vec{p}_k^{GB}\|} \ .
$$

Algorithm 1 describes the proposed optimization method.

Algorithm 1 GB optimization

Require: Initial point $\vec{x}_0$ and a tolerance ε.
  1: Initialize $H_0 = I$
  2: $\vec{P}_k^{GB} = -\nabla f(\vec{x}_0)$
  3: Set $k = 0$
  4: **while** $\|\nabla f(\vec{x}_k)\| > \varepsilon$ **do**
  5:   $\vec{P}_k^{GB} = \frac{\vec{p}_k^{GB}}{\|\vec{p}_k^{GB}\|}$
  6:   Compute the step size α_k to satisfy the Wolfe Conditions (Eqs. 7 and 8)
  7:   $\vec{x}_{k+1} = \vec{x}_k + \alpha_k \vec{P}_k^{GB}$
  8:   $\vec{s}_k = \vec{x}_{k+1} - \vec{x}_k$
  9:   $\vec{y}_k = \nabla f(\vec{x}_k + 1) - \nabla f(\vec{x}_k)$
 10:   $\rho_k = \frac{1}{\vec{y}_k^T \vec{s}_k}$
 11:   $H_{k+1} = (I - \rho_k \vec{s}_k \vec{y}_k^T)H_k(I - \rho_k \vec{y}_k \vec{s}_k^T) + \rho_k \vec{s}_k \vec{s}_k^T$
 12:   $\vec{p}_{k+1}^{GB} = -[\psi(\rho_k)H_k \nabla f(\vec{x}_k) + (1 - \psi(\rho_k))\nabla f(\vec{x}_k)]$
 13:   Set $k = k + 1$
 14: **end while**

E. Implementation details

1) Initial point: Our proposed cost function has a trivial solution at the point $\vec{C} = [0, 0, ..., 0]$. Therefore, we define the initial point for the first frame to be segmented by setting the offset coefficient α_0 to be equal to the mean of the radial coordinates of the blood samples given by the user, while the rest of the coefficients are set to $\{\alpha_i, \beta_i\} = 0.1 \; \forall \; i > 0$. Since it is very likely that the shape of the lumen on consecutive frames is is similar, we use the resulting segmentation curve of each frame as the initial point (one near to the solution) for the next frame. This improves the algorithm convergence rate.

2) Robustness to changes of appearance: Due to changes in the speed of the blood flow, it is possible to observe significant differences between the textures on the lumen of the frames in the same sequence and then our assumption of similarity of textures among frames does not hold. Moreover, the visualization parameters of the IVUS system may be changed during the IVUS intervention causing large variability on the appearance of the IVUS frames of the same sequence. Hence, it may be possible that the predicting SVM model that was computed using samples from the first frame is not reliable for predicting the other frames. To overcome this limitation, we propose to check the reliability of prediction of each frame before using it as likelihood. For this, we part from the assumption that the shape of the lumen for consecutive frames is similar. Consider the lumen curve result from a frame $\mathbf{S}_i$. If we place this curve on the next frame $i + 1$, most of the pixels above the curve corresponds to blood while those below the curve correspond to non-blood with an exception on those pixels near the curve considering the catheter was not undergoing a large rotation (this case will be discussed later). We create a mask by placing a "inactive band" of a fixed width w_b around this contour; we can consider all the pixels above S_1 contour as class lumen. However, for the pixels below the contour, we are most interested in those that correspond to vessel wall or plaque. Since it is very likely that the pixels below this contour include other kinds of tissues apart from those in which we are interested, we take only a narrow band of width w_n below S_i and we consider those pixels as non-lumen (Fig. 11). We compute the texture energies for the frame $i + 1$ and we perform the classification of all its pixels. We compare the accuracy on the classification of those pixels belonging to the mask considering as ground truth the class defined by it. If the accuracy of the classification is above a given threshold (i.e., $\geq \tau_1\%$), then we assume that we can trust the prediction and therefore assign the likelihoods for this frame. If the accuracy is below this threshold, we build a new training set consisting of ξ_2 of the original training set samples and ξ_3 of the samples corresponding to the mask chosen randomly. We perform the grid search and cross-validation for finding the new optimal parameters for the SVM and we evaluate the accuracy of the prediction using all the samples given by the mask. If the accuracy is above the threshold we use this new model for performing the classification and likelihood estimation of the frame. If the accuracy is below this threshold, it is very likely that this is because there are samples with similar texture features for blood and non-blood due to a rotation of the catheter and not because of a change of appearance on the textures. In this case we keep the original class prediction and use it as likelihoods. Figure 10 depicts the block diagram of our segmentation method.

F. Sensitivity analysis

As mentioned before, the sharpness of the transition between classes is controlled by the parameter λ. The value of this parameter may have an impact in the precision of the segmentation curve. On the other hand, the number of Fourier coefficients N_k determines the smoothness of the curve. To evaluate the sensitivity of our method with respect to these parameters, we have performed segmentation of the first five frames from six 20 MHz and six 40 MHz IVUS sequences (60 frames in total) using different values for λ and N_k, and we compute the similarity of the results with the manual segmentation by an expert observer employing the Dice similarity coefficient which, for a two sets A and B is given by [34]:

$$D(A, B) = \frac{2|A \cap B|}{|A| + |B|}$$

Figure 11(a) depicts the result of the sensitivity analysis with respect to λ using $N_k = 5$ while Fig. 11(b) depicts the results of the sensitivity analysis with respect to N_k employing $\lambda = 0.5$. As we can observe, our method is robust with respect to the value of λ, while the segmentation result remains approximately constant when $\lambda \geq 0.3$. Similarly, we can observe that our method is also robust with respect to the number of Fourier coefficients, with the best results when $N_k \leq 7$.
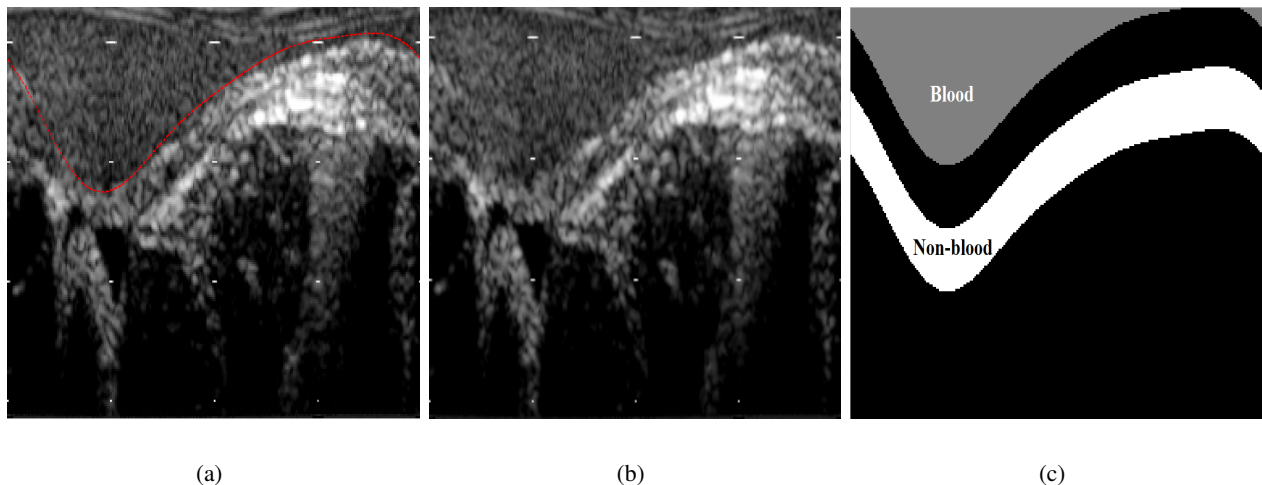
Fig. 9. Example of (a) the lumen segmentation result of a frame, (b) the next consecutive frame, and (c) the regions considered as blood and non-blood.
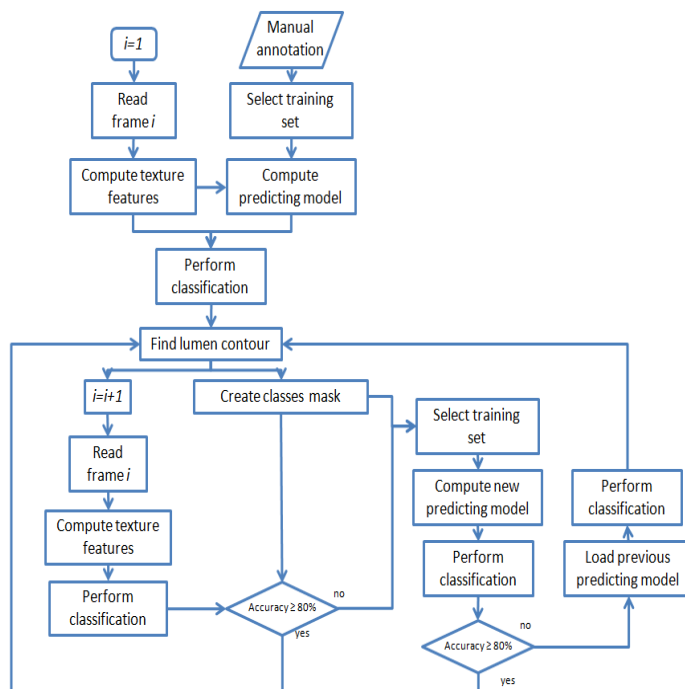

Fig. 10. Block diagram of our segmentation method.

IV. RESULTS

The method proposed in this paper was implemented using MATLAB®, and we performed automatic segmentation of frames from 20 MHz and 40 MHz IVUS pullback sequences using $\lambda = 0.4$, and $N_k = 5$ as these values report good stability on the sensitivity analysis. The rest of the parameters were experimentally set to $\xi_1 = \xi_3 = \frac{1}{20}$, $\xi_2 = \frac{1}{10}$, $\tau_1 = 80$, $w_b = 20$, and $w_n = 50$. The performance of our method was evaluated by comparing our segmentation results with the manual segmentation of the same frames by one expert observer. Specifically, we computed the Dice similarity coefficient between our segmentation method and the expert segmentation. The agreement between the areas corresponding to lumen according to each segmentation was evaluated using linear regression, coefficient of determination and Bland-Altman analysis [35]. Additionally, we compared the performance of our method with the performance of three recent existing IVUS segmentation methods proposed by Unal *et al.* [17], Papadogiorgaki *et al.* [20], and Katouzian *et al.* [21] for which we perform the same evaluations. The
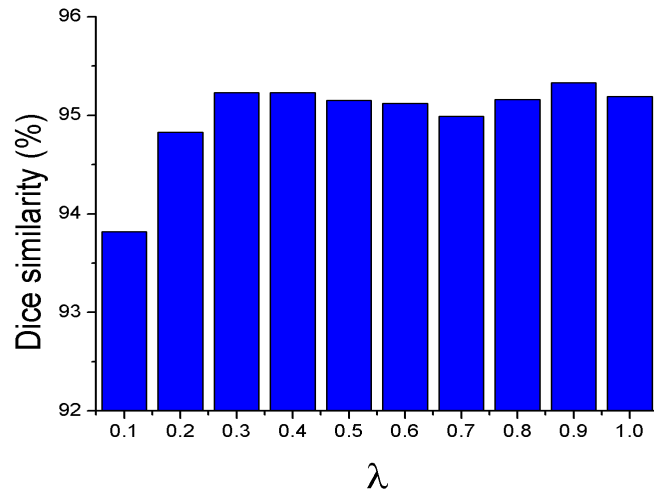
(a)
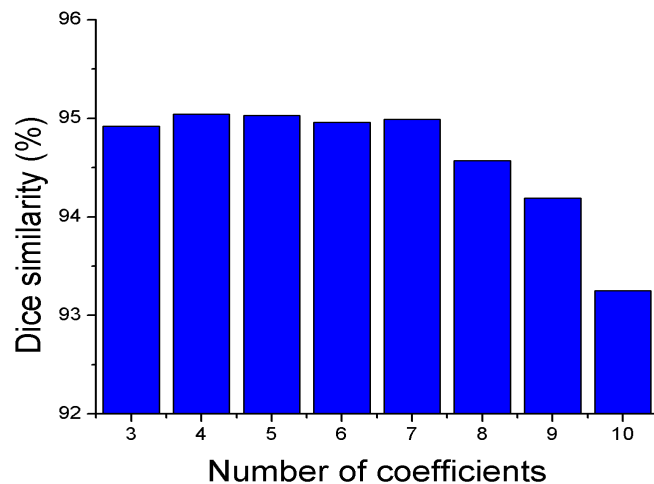
(b)

Fig. 11. Sensitivity analysis for (a) λ and (b) N_k.

information about the IVUS sequences and the number of segmented frames for each method is listed in Table II. The number of times the model was computed along with its total time, and the average time for segmenting each frame are listed in Table IV. The mean Dice similarity and standard deviation results for the comparison of each automatic method segmentation with manual segmentation from an expert observer for each sequence are depicted as a box plot in Fig 12, and the results are listed in Table IV. Figures 13, 14, 15, and 16 depict the coefficient of determination, linear regression, and Bland-Altman plots for the comparison of the lumen areas with the expert observer segmentation of all the sequences for all the methods. Finally, Figs. 17 and 18 depict examples of the segmentation results for each method along with the segmentation by the expert observer.

TABLE II

INFORMATION ABOUT THE IVUS SEQUENCES AND THE NUMBER OF SEGMENTED FRAMES FOR OUR METHOD (MKR), UNAL'S METHOD (UNL), PAPADOGIORGAKI'S METHOD (PAP), AND KATOUZIAN'S METHOD (KAT).

Sequence information		Number of segmented frames			
ID	Frequency	MKR	UNL	PAP	KAT
1	20 MHz	50	50	50	48
2	20 MHz	50	50	50	0
3	20 MHz	50	50	50	0
4	20 MHz	50	50	50	0
5	20 MHz	50	48	50	0
6	20 MHz	50	49	50	0
7	40 MHz	50	50	50	48
8	40 MHz	50	50	50	48
9	40 MHz	50	50	50	48
10	40 MHz	50	50	50	48
11	40 MHz	50	50	50	48
12	40 MHz	35	35	35	32

TABLE III

AVERAGE SEGMENTATION TIME PER FRAME (ST), NUMBER OF TIMES THAT THE MODEL WAS COMPUTED (MT), AND TOTAL MODEL COMPUTATION TIME (TT) FOR EACH SEQUENCE.

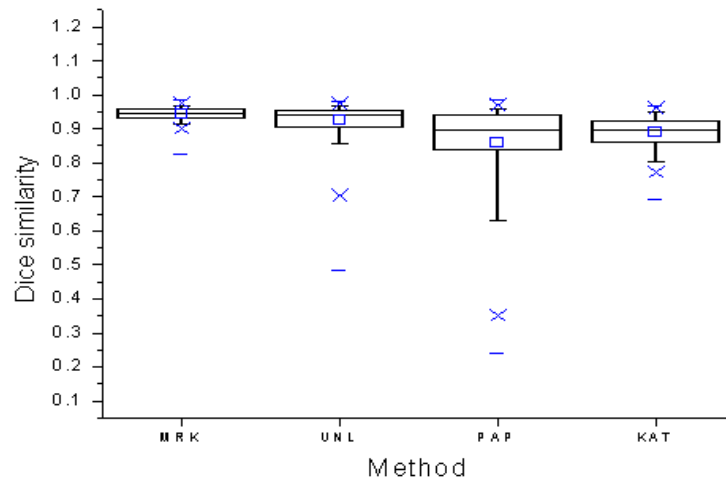| ID	ST	MT	TT
1	3.04	1	3.38
2	3.43	1	4.13
3	3.42	1	3.21
4	3.14	1	7.23
5	2.71	1	2.38
6	4.21	1	9.45
7	5.11	1	8.52
8	7.08	2	33.2
9	5.75	1	9.54
10	5.15	2	24.31
11	5.16	1	13.12
12	4.55	1	13.02

Fig. 12. Box plot of the Dice similarity coefficient for the comparison of the segmentation results of our method (MKR), Unal's method (UNL), Papadogiorgaki's method (PAP), and Katouzian's method (KAT), with the manual segmentation for all frames of all sequences.

TABLE IV

Mean Dice similarity and standard deviation (std) results for the comparison of the segmentation results of our method (MKR), Unal's method (UNL), Papadogiorgaki's method (PAP), and Katouzian's method (KAT), with manual segmentation from an expert observer for each sequence (N.A. stands for not available).

	MKR		UNL		PAP		KAT	
ID	Mean (%)	std	Mean (%)	std	Mean (%)	std	Mean (%)	std
1	92.66	0.83	90.24	1.80	70.87	3.52	82.73	4.19
2	93.16	1.22	90.87	1.79	85.90	2.80	N.A.	N.A.
3	94.44	1.18	93.26	2.75	89.55	2.78	N.A.	N.A.
4	94.20	1.66	96.25	1.02	94.66	0.89	N.A.	N.A.
5	94.30	2.03	94.79	4.30	92.69	10.11	N.A.	N.A.
6	93.89	0.91	95.99	1.79	91.07	2.24	N.A.	N.A.
7	95.35	1.28	95.59	1.17	86.64	4.03	90.21	3.38
8	95.63	1.12	91.16	9.56	64.79	16.06	89.32	4.07
9	94.77	1.96	91.22	2.42	90.04	6.11	88.92	2.24
10	92.50	2.55	88.33	8.31	91.23	4.80	88.69	3.94
11	93.63	1.92	93.52	1.10	91.97	2.51	93.32	2.17
12	96.70	0.92	95.32	1.08	95.23	2.75	89.49	2.50
Average	**94.27**	**1.47**	**93.05**	**3.09**	**87.05**	**4.88**	**88.96**	**3.38**

A. Results on a sequence with changes of appearance

To evaluate the robustness of our method with respect to changes in the visualization parameters and catheter rotations, we have performed an experiment using a modified version of Sequence 7 where we have performed a $90°$ rotation and changes in the intensity and contrast every 10 frames. Figure 19 depicts the segmentation result on the first frame of each modified subsequence. In this case the average frame segmentation time was 4.51 sec., the model was computed 4 times, and the total model computation time was 63.88 sec. The mean Dice similarity of the comparison with the manual segmentation was 92.84% with a standard deviation of 2.19%.

## B. Results on IVUS images with artifacts

Shadows may appear on the IVUS images due to calcified plaque, echo loss, and other low acoustic impedance tissues outside the vessel. This artifact may hamper the segmentation result due to the similarity of texture and intensity to the lumen region, especially for 20 MHz IVUS sequences. Figure 20 depicts the segmentation result using our method on images that present shadow artifacts in 20 MHz and 40 MHz.

Guidewire artifacts can appear as a bright spot or a bright area near the catheter. This artifact may also generate shadows in the radial direction. Due to the intensity of this artifact being similar to the intensity of wall tissue, it can be incorrectly segmented as part of the wall. Moreover, the shadow generated by the guidewire may mislead the contour towards an incorrect segmentation. Figure 21 depicts the segmentation result using our method on images that present guidewire artifacts in 20 MHz and 40 MHz.

C. Limitations

Side branches are identified as the opening formed when the vessel being imaged bifurcates. This is visualized as an area with similar intensity values and texture extending from the lumen in the near field towards the far field; this represents a challenge for any active-contour based segmentation method because the segmenting contour could advance through this shadow and lead to an incorrect segmentation of the luminal border. Since small side branches have an effect similar to that of guidewire artifacts, our method will be able to overcome this problem. However, for large side branches our method will incorrectly move the contour towards the branch since it is designed to keep inside the contour as much region with texture of blood as possible (Fig. 22).

Our method may fail in cases in which the texture features of the lumen in a frame are very similar to those of a region of the vessel wall. Normally, these cases are difficult even for the expert observers. However, this happens rarely and in general our method is able to correctly segment even in these cases of similar texture features. Figure 23 depicts an example of two frames of a 40 MHz sequence in which the texture of the lumen is similar to the texture of a region of the wall. In this sequence, most of the frames were correctly segmented. However, for some frame in which the texture features were extremely similar, our method performed an incorrect segmentation.
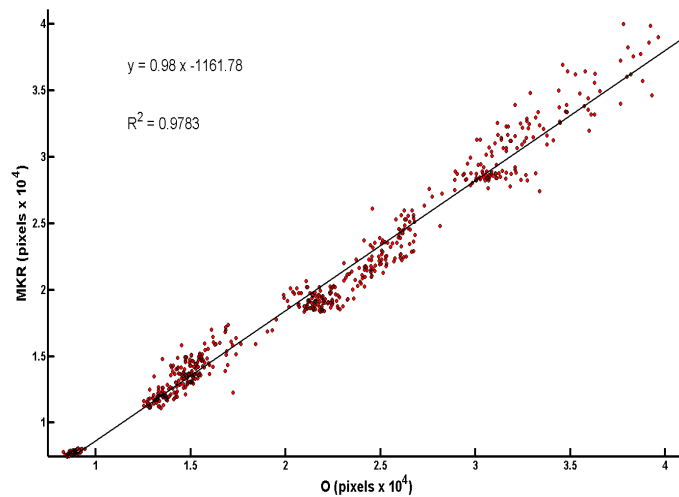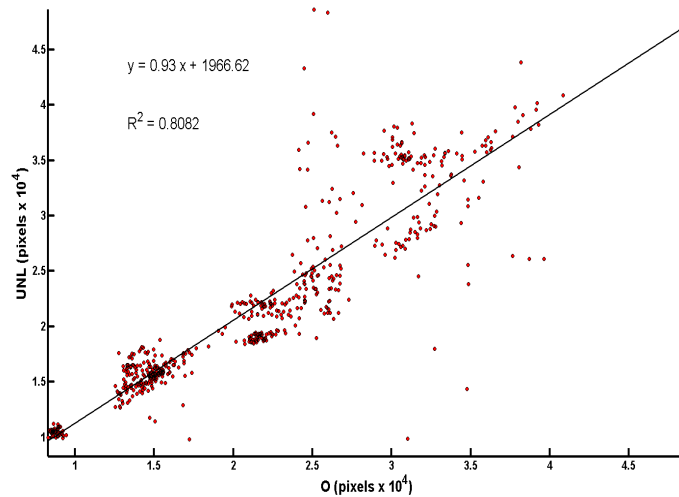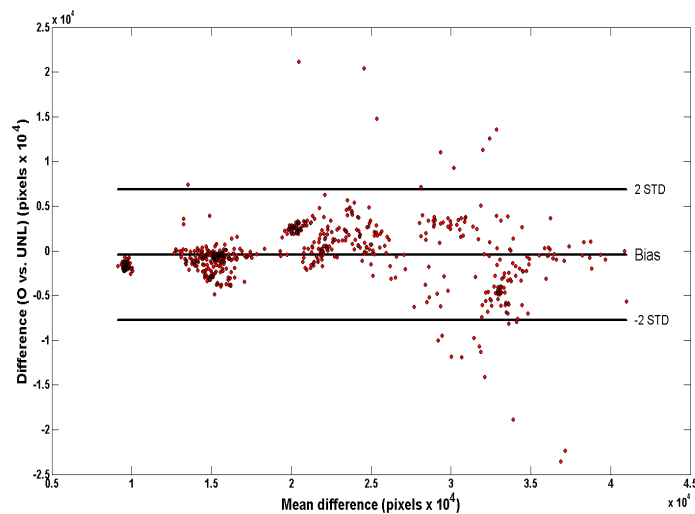
(a)
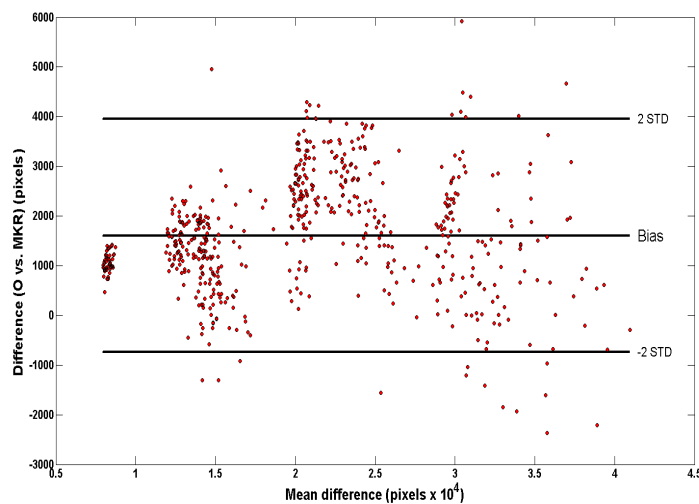
(b)

Fig. 13. (a) Linear regression and (b) Bland-Altman plot for the comparison of the lumen areas between our method and the expert observer for all sequences.

V. DISCUSSION

The linear regression depicts a better agreement for our method, and higher coefficient of determination when compared with the other methods. Similarly, the Bland-Altman analysis showed a low bias and less dispersion than these previous methods. While the average Dice similarity results of our method and Unal's method are comparable, our method presents a consistently smaller standard deviation which means that our method is more stable (this can also be observed by comparing the linear regression and Bland-Altman plots). Moreover, in contrast to Unal's method, our method is robust with respect to its parameters λ and N_k and does not require any supervised parameter tuning or training when changing between sequences with different IVUS frequencies or visualization parameters. Regarding large side-branches, we believe that our method can overcome this limitation by implementing the pre-processing step for side-branches proposed by Unal *et al.* [17] in which side branches are detected prior to
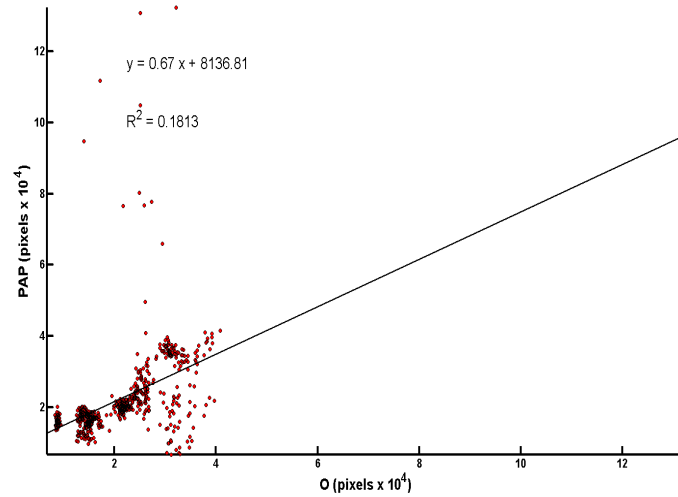
(a)

(b)

Fig. 14. (a) Linear regression and (b) Bland-Altman plot for the comparison of the lumen areas between Unal's method and the expert observer for all sequences.

the segmentation process. We have not included this step in this work since we want to present exclusively our approach. Most of the frame segmentation time is used by the computation of the Law's texture energies. However, considering that this code was implemented in a MATLAB®, we believe that the segmentation process time can be dramatically reduced by implementing the method using a lower level language such as C++.

VI. CONCLUSION

We have presented a robust probabilistic approach for the segmentation of the luminal border on IVUS images. Our method incorporates texture information by using the prediction of an SVM classifier model. This step allows our method to auto calibrate, which enables segmentation of IVUS images from different frequencies (i.e., 20 and 40 MHz) without the need of adjusting any parameter, and it makes our method robust to the problem of variability
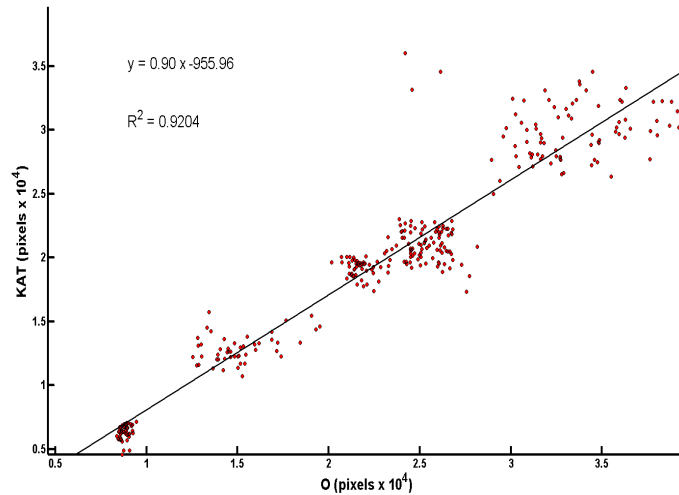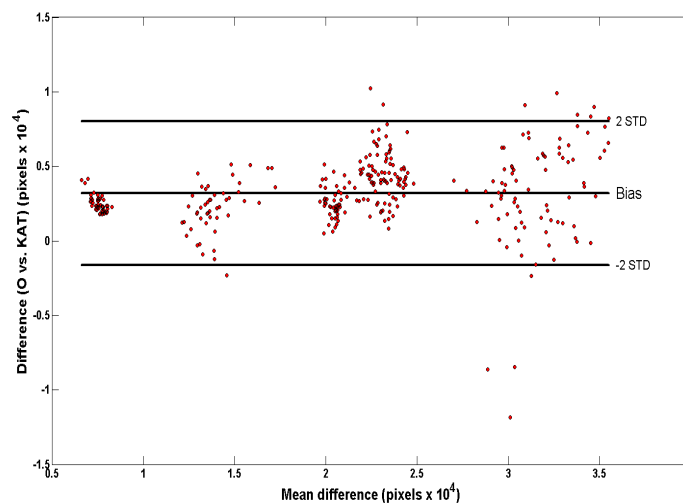
(a)
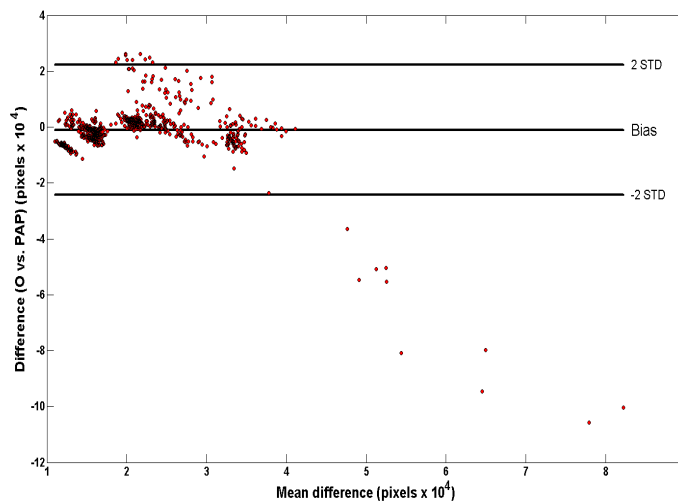
(b)

Fig. 15.   (a) Linear regression and (b) Bland-Altman plot for the comparison of the lumen areas between Papadogiorgaki's method and the expert observer for all sequences.

of IVUS image appearance. In addition, our method includes a step in which changes in appearance within the sequence are automatically detected and the SVM model is adjusted. Moreover, the probabilistic formulation of our method overcomes most of the limitations related to artifacts such as catheter rotations, shadows, speckle noise, and guidewire artifacts. Our proposed GB optimization has been shown to be well suited for this type of problem because it is faster than the steepest descent optimization, and at the same time it can be controlled to avoid large steps that lead to an incorrect segmentation. The results indicate that the performance of our method is superior when compared with other existing methods. To the best of our knowledge, this is the first method to be robust with respect to changes on IVUS image appareance and within-sequence visualization parameter changes. Finally segmentation of media/adventitia border is subject of future work.

(a)

(b)

Fig. 16.   (a) Linear regression and (b) Bland-Altman plot for he comparison of the lumen areas between Katouzian's method and the expert observer for all sequences.

REFERENCES

[1] D. Lloyd-Jones, R. Adams, M. Carnethon, G. De Simone, T. B. Ferguson, K. Flegal, E. Ford, K. Furie, A. Go, K. Greenlund, N. Haase, S. Hailpern, M. Ho, V. Howard, B. Kissela, S. Kittner, D. Lackland, L. Lisabeth, A. Marelli, M. McDermott, J. Meigs, D. Mozaffarian, G. Nichol, C. O'Donnell, V. Roger, W. Rosamond, R. Sacco, P. Sorlie, R. Stafford, J. Steinberger, T. Thom, S. Wasserthiel-Smoller, N. Wong, J. Wylie-Rosett, and Y. Hong, "Heart disease and stroke statistics-2009 update: A report from the American Heart Association statistics committee and stroke statistics subcommittee." *Circulation*, vol. 119, no. 3, pp. 480–486, 2009.
[2] D. S. Meier, R. M. Cothren, D. G. Vince, and J. F. Cornhill, "Automated morphometry of coronary arteries with digital image analysis of intravascular ultrasound," *American Heart Journal*, vol. 133, no. 6, pp. 681–690, Jun. 1997.
[3] E. Mendizabal-Ruiz, M. Rivera, and I. Kakadiaris, "A probabilistic segmentation method for the identification of luminal borders in intravascular ultrasound images," in *Proc. IEEE Computer Society Conference on Computer Vision and Pattern Recognition*, Anchorage, AK, Jun. 24-26 2008, pp. 1–8.
[4] M. Sonka, X. Zhang, M. Siebes, M. Bissing, S. DeJong, and S. Collins, "Segmentation of intravascular ultrasound images: A knowledge-based approach," *IEEE Transactions on Medical Imaging*, vol. 14, no. 4, pp. 719–732, Dec. 1995.
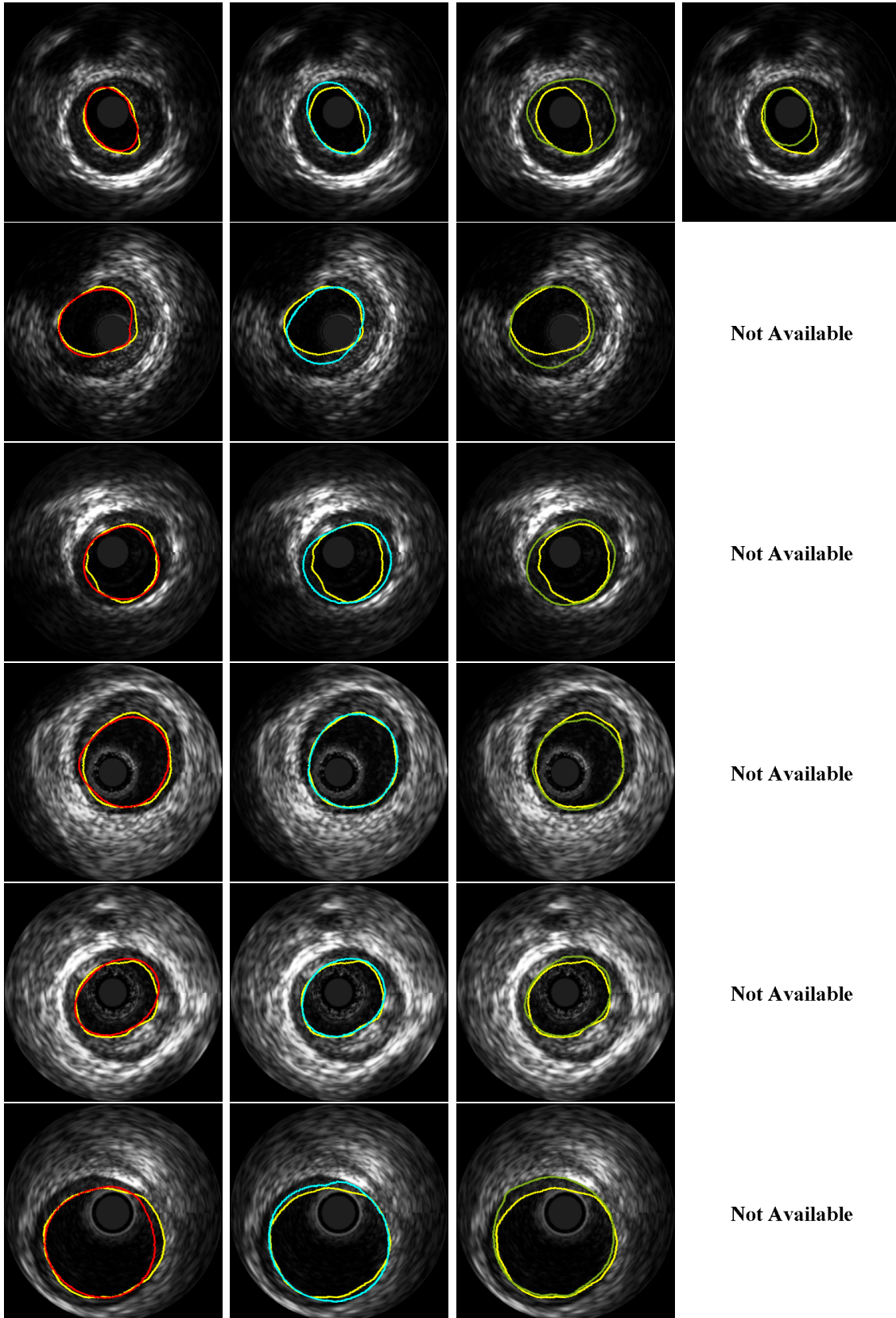
Fig. 17. Examples of automatic segmentation results for 20 MHz sequences along with the segmentation of the expert observer (yellow line). From left to right the images correspond to MKR, UNL, PAP, and KAT, respectively.
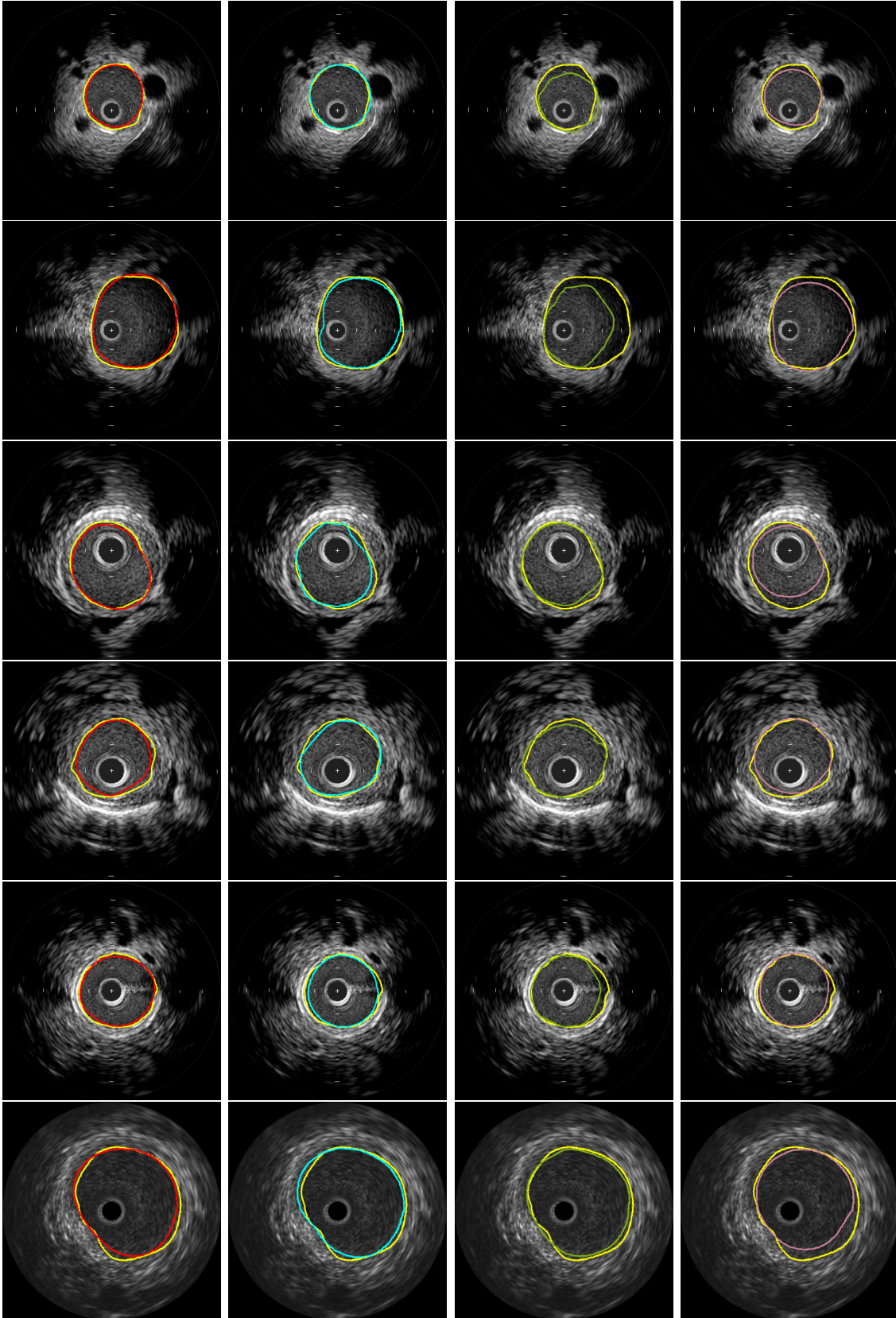
Fig. 18. Examples of automatic segmentation results for 40 MHz sequences along with the segmentation by the expert observer (yellow line). From left to right the images correspond to MKR, UNL, PAP, and KAT, respectively.
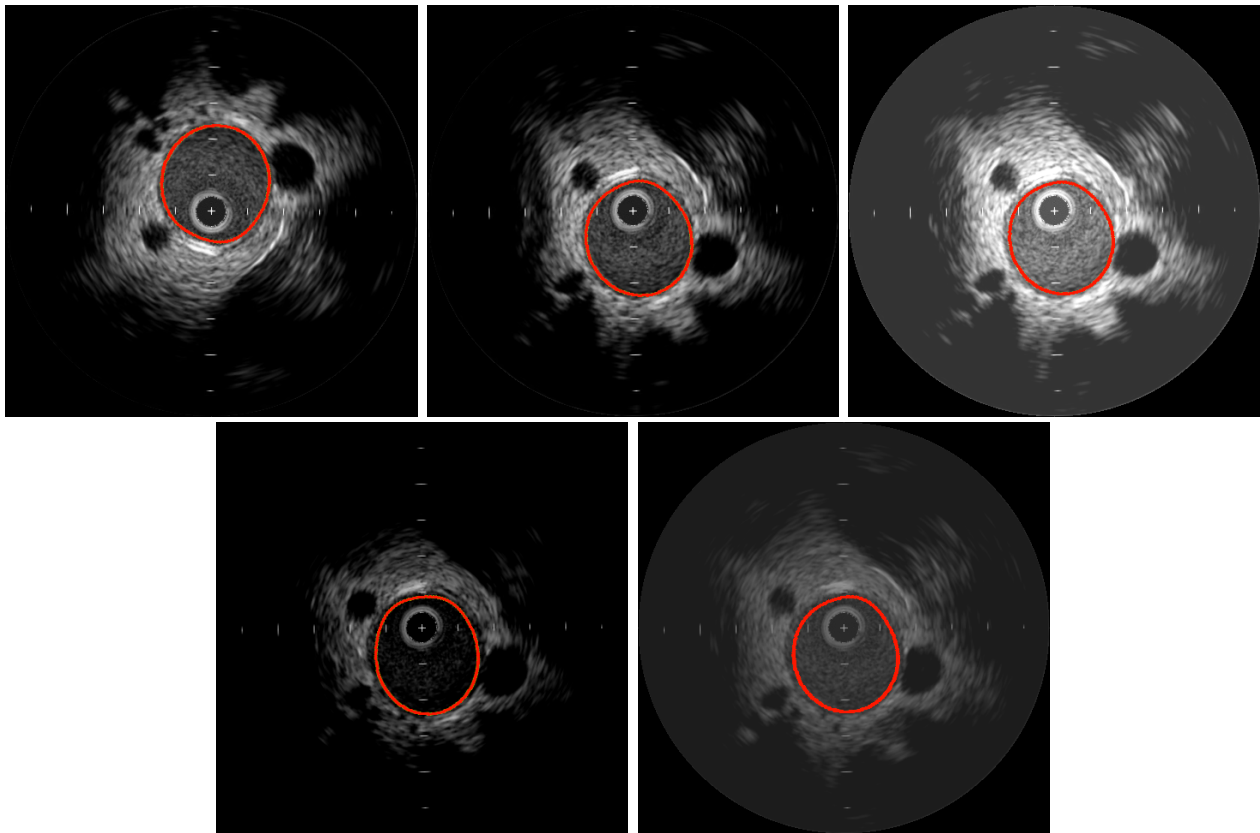
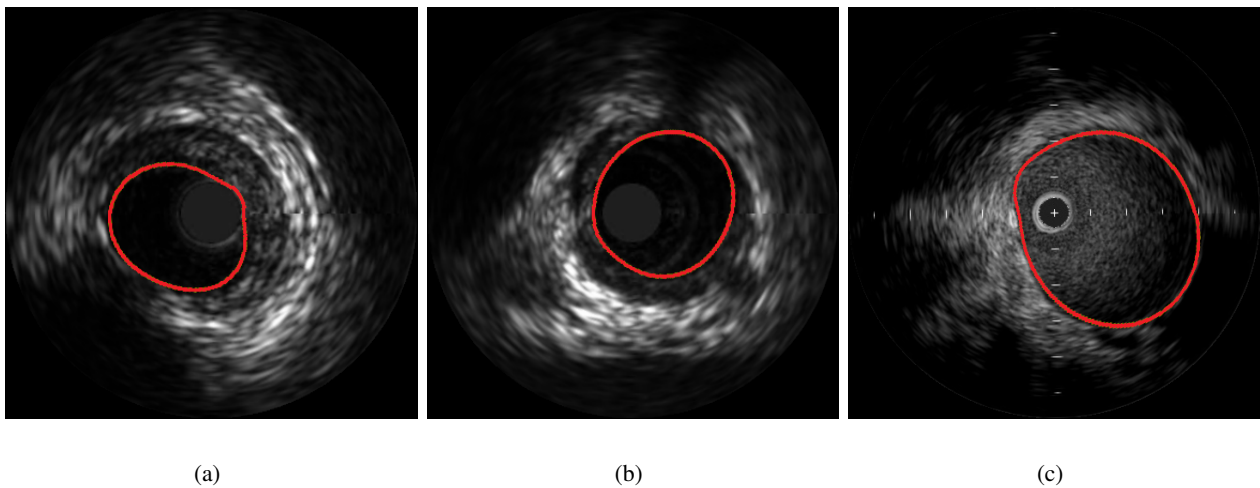Fig. 19. Segmentation results on the first frame of each modified subsequence.

(a)   (b)   (c)

Fig. 20. Segmentation example of (a, b) 20 MHz and (c) 40 MHz IVUS images with shadow artifacts.

[5] C. von Birgelen, C. Mario, W. Li, J. Schuurbiers, C. Slager, P. de Feyter, P. Serruys, and J. Roelandt, "Morphometric analysis in three-dimensional intracoronary ultrasound: An in vitro and in vivo study using a novel system for the contour detection of lumen and plaque," *American Heart Journal*, vol. 132, no. 2, pp. 516–527, 1996.

[6] X. Zhang, C. McKay, and M. Sonka, "Tissue characterization in intravascular ultrasound images," *IEEE Transactions on Medical Imaging*, vol. 17, no. 6, pp. 889–899, Dec. 1998.

[7] J. Klingensmith, R. Shekhar, and D. Vince, "Evaluation of three-dimensional segmentation algorithms for the identification of luminal and medial-adventitial borders in intravascular ultrasound images," *IEEE Transactions on Medical Imaging*, vol. 19, no. 10, pp. 996–1011, 2000.

[8] G. Kovalski, R. Beyar, R. Shofti, and H. Azhari, "Three-dimensional automatic quantitative analysis of intravascular ultrasound images," *Ultrasound in Medicine and Biology*, vol. 26, no. 4, pp. 527–537, 2000.
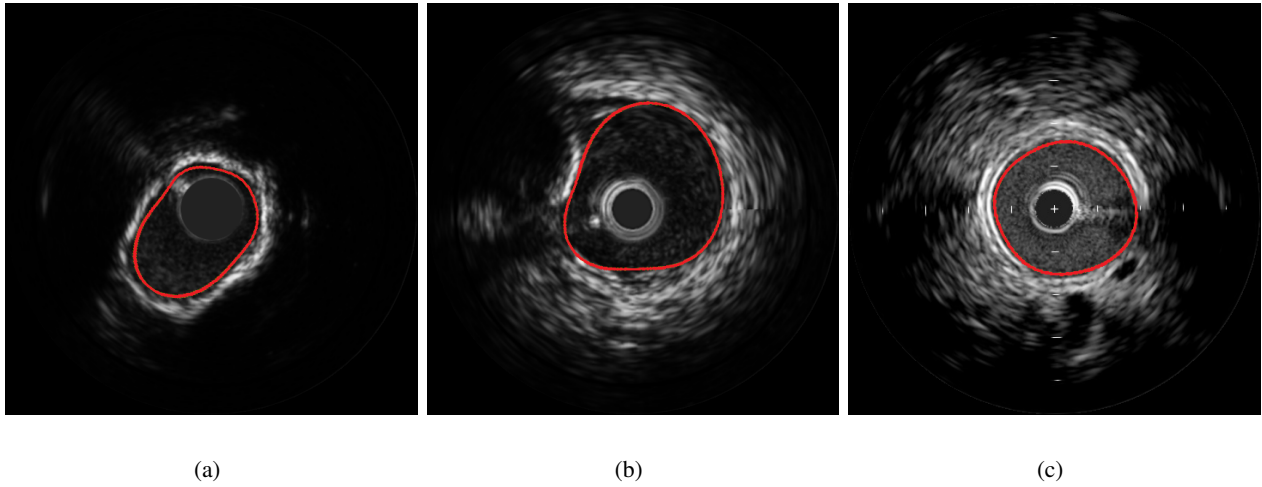
(a) (b) (c)

Fig. 21.   Segmentation example of (a, b) 20 MHz and (c) 40 MHz IVUS images with shadow artifacts.
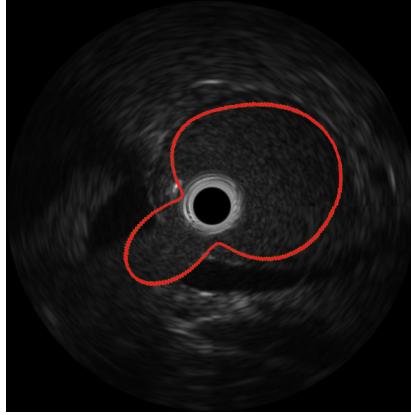

Fig. 22.   Example of an IVUS frame with a side branch on which our method fails.
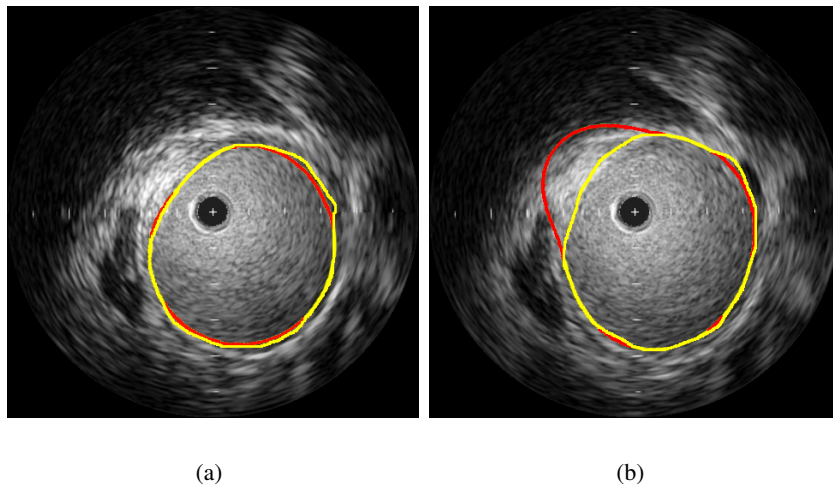

(a) (b)

Fig. 23.   Example of two frames of a 40 MHz sequence on which the texture of the lumen is similar to the texture of a region of the wall. The red line corresponds to the automatic segmentation, while the yellow line corresponds to the manual segmentation by the expert observer.

[9] M. Plissiti, D. Fotiadis, L. Michalis, and G. Bozios, "An automated method for lumen and media-adventitia border detection in a

sequence of IVUS frames," *IEEE Transactions on Information Technilogy in Biomedicine*, vol. 8, no. 2, pp. 131–141, Jun. 2004.

[10] A. Mojsilovic, M. Popovic, N. Amodaj, R. Babic, and M. Ostojic, "Automatic segmentation of intravascular ultrasound images: A texture-based approach," *Annals of Biomedical Engineering*, vol. 25, no. 6, pp. 1059–1071, Nov. 1997.

[11] C. Haas, H. Ermert, S. Holt, P. Grewe, A. Machraoui, and J. Barmeyer, "Segmentation of 3D intravascular ultrasonic images based on a random field model," *Ultrasound in Medicine and Biology*, vol. 26, no. 2, pp. 297–306, 2000.

[12] Z. Luo, Y. Wang, and W. Wang, "Estimating coronary artery lumen area with optimization-based contour detection," *IEEE Transactions on Medical Imaging*, vol. 22, pp. 564–546, Apr. 2003.

[13] H. Hui-Zhu, Y. Liang, and M. Friedman, "IVUS image segmentation based on contrast," in *Proc. SPIE Medical Imaging: Image Processing*, vol. 4684, 2002, pp. 1727–1733.

[14] E. Brusseau and C. de Korte, "Fully automatic luminal contour segmentation in intracoronary ultrasound imaging - a statistical approach," *IEEE Transactions on Medical Imaging*, vol. 23, no. 5, pp. 554–566, May 2004.

[15] M. Cardinal, J. Meunier, G. Soulez, R. Maurice, E. Therasse, and G. Cloutier, "Intravascular ultrasound image segmentation: A three-dimensional fast-marching method based on gray level distributions," *IEEE Transactions on Medical Imaging*, vol. 25, no. 5, pp. 590–601, 2006.

[16] E. dos Santos Filho, M. Yoshizawa, A. Tanaka, and Y. Saijo, "A study on intravascular ultrasound image processing," *Record of Electrical and Communication Engineering Conversazione, Tohoku University*, vol. 74, no. 2, pp. 30–33, 2006.

[17] G. Unal, S. Bucher, S. Carlier, G. Slabaugh, T. Fang, and K. Tanaka, "Shape-driven segmentation of the arterial wall in intravascular ultrasound images," *IEEE Transactions on Information Technology in Biomedicine*, vol. 12, no. 3, pp. 335–347, May 2008.

[18] A. Taki, Z. Najafi, A. Roodaki, S. Setarehdan, R. Zoroofi, A. Konig, and N. Navab, "Automatic segmentation of calcified plaques and vessel borders in IVUS images," *International Journal of Computer Assisted Radiology and Surgery*, vol. 3, no. 3-4, pp. 347 – 354, 2008.

[19] R. Downe, A. Wahle, T. Kovarnik, H. Skalicka, J. Lopez, J. Horak, and M. Sonka, "Segmentation of intravascular ultrasound images using graph search and a novel cost function," in *Proc. 2nd MICCAI Workshop on Computer Vision for Intravascular and Intracardiac Imaging*, New York, NY, Sep. 10 2008, pp. 71–79.

[20] M. Papadogiorgaki, V. Mezaris, Y. Chatzizisis, G. Giannoglou, and I. Kompatsiaris, "Image analysis techniques for automated IVUS contour detection." *Ultrasound in Medicine and Biology*, vol. 34, no. 9, pp. 1482–1498, Sep. 2008.

[21] A. Katouzian, B. Baseri, E. Konofagou, and A. Laine, "Automatic detection of blood versus non-blood regions on intravascular ultrasound (IVUS) images using wavelet packet signatures," in *Proc. Proceedings of SPIE Medical Imaging 2008: Ultrasonic Imaging and Signal Processing*, San Diego, CA, Feb. 16 - 21 2008.

[22] F. Ciompi, O. Pujol, E. Fernandez-Nofrerias, J. Mauri, and P. Radeva, "ECOC random fields for lumen segmentation in radial artery IVUS sequences," in *Proc. Proceedings of 12th International Conference on Medical Image Computing and Computer Assisted Intervention*, London, UK, Sep. 20 - 24 2009, pp. 869–876.

[23] M. Wennogle and W. Hoff, "Three dimensional segmentation of intravascular ultrasound data," in *Proc. 6th International Conference on Image Analysis and Recognitio*, Toronto, Canada, 2009, pp. 772–781.

[24] M. Cardinal, G. Soulez, J. Tardif, J. Meunier, and G. Cloutier, "Fast-marching segmentation of three-dimensional intravascular ultrasound images: A pre-and post-intervention study," *Medical physics*, vol. 37, no. 7, pp. 3633–3647, 2010.

[25] T. Hiro, C. Leung, R. Russo, H. Karimi, A. Farvid, and J. Tobis, "Variability of a three-layered appearance in intravascular ultrasound coronary images: A comparison of morphometric measurements with four intravascular ultrasound systems," *American Journal of Cardiac Imaging*, vol. 10, no. 4, pp. 219–227, 1996.

[26] G. Mintz, S. Nissen, W. Anderson, S. Bailey, R. Erbel, P. Fitzgerald, F. Pinto, K. Rosenfield, R. Siegel, E. Tuzcu, and P. Yock, "American College of Cardiology clinical expert consensus document on standards for acquisition, measurement and reporting of intravascular ultrasound studies (IVUS)," *Journal of the American College of Cardiology*, vol. 37, no. 5, pp. 1478–1492, 2001.

[27] M. Rivera, O. Ocegueda, and J. L. Marroquin, "Entropy-controlled quadratic Markov measure field models for efficient image segmentation," *IEEE Transactions on Image Processing*, vol. 16, pp. 3047–3057, Aug. 2007.

[28] T. S. D. Lee, "Image segmentation from texture measurement," *ISPRS Journal of Photogrammetry and Remote Sensing*, vol. 29, pp. 195–199, August 1992.

[29] K. I. Laws, "Rapid texture identification," in *Proc. SPIE Conference on Image Processing for Missile Guidance*, 1980, pp. 376–380.

[30] C. Burges, "A tutorial on support vector machines for pattern recognition," *Data Mining and Knowledge Discovery*, vol. 2, no. 2, pp. 121–167, 1998.

[31] H. Lin, C. Lin, and R. Weng, "A note on platt's probabilistic outputs for support vector machines," *Machine Learning*, vol. 68, no. 3, pp. 267–276, 2007.

[32] C.-C. Chang and C.-J. Lin, "LIBSVM: A library for support vector machines," 2001, software available at http://www.csie.ntu.edu.tw/.

[33] J. Nocedal and S. Wright, *Numerical Optimization*. Springer, 1999.

[34] C. J. v. Rijsbergen, *Information retrieval*. London: Butterworths, 1979.

[35] J. Bland and D. Altman, "Statistical methods for assessing agreement between two methods of clinical measurement," *Lancet*, vol. 1, no. 8476, pp. 307–310, Feb. 1986.